Dynamic simulation of hydrogen trapping in bifurcating water-wet microchannels using the lattice Boltzmann method

van Rooijen, Willemijn A.; Fu, Pengyu; Wang, Yuhang; Hajibeygi, Hadi

DOI
10.1016/j.ijhydene.2025.151274

Publication date
2025

Document Version
Final published version

Published in
International Journal of Hydrogen Energy

International Journal of Hydrogen Energy 177 (2025) 151274

Contents lists available at ScienceDirect

International Journal of Hydrogen Energy

journal homepage: www.elsevier.com/locate/he

Dynamic simulation of hydrogen trapping in bifurcating water-wet microchannels using the lattice Boltzmann method

Willemijn A. van Rooijen [a], Pengyu Fu [b], Yuhang Wang [b,*], Hadi Hajibeygi [a]

[a] Reservoir Engineering, Geoscience and Engineering Department, Faculty of Civil Engineering and Geosciences, Delft University of Technology, Delft, The Netherlands

[b] School of Environmental Studies, China University of Geosciences (Wuhan), Wuhan, China

ARTICLE INFO

Keywords:
Underground hydrogen storage
Residual trapping
Pore-scale simulation
Pore doublet model
Lattice Boltzmann method

ABSTRACT

Residual trapping is a critical mechanism influencing the efficiency of Underground Hydrogen Storage (UHS). This study investigates the underlying processes of residual trapping by bypassing, through bifurcating geometries, focusing on how geometrical parameters and flow characteristics affect the trapping process. We develop a dynamic simulation framework based on the lattice Boltzmann method (LBM) to simulate full drainage/imbibition cycles. Various geometries, based on the pore doublet model, were investigated and supported by theoretical analysis. In addition, trapping behavior of hydrogen was compared to that of CO_2 and CH_4. It is found that the channel width ratio, specially across the local bifurcating geometries, and the roundness of the grains, are among the key factors which control hydrogen trapping. Results indicate that the suited reservoirs for underground hydrogen storage have narrower channel-size ratios and smoother edges at micro-scale. Operational conditions also play a significant role. Lower flow rates enhance bypassing, which increases trapping.

1. Introduction

For a successful transition towards net-zero goals, it is crucial to upscale green energy systems, from production to transportation and specially storage [1–4]. Hydrogen, H_2, with its high gravimetric energy density and clean combustion products, can be a remedy to the long-standing challenge of TWh-scale energy storage [5–7]. Indeed, hydrogen can be stored in large quantities in geological formations, such as depleted hydrocarbon reservoirs, aquifers, and salt caverns [8–12].

The efficiency of underground hydrogen storage (UHS) in porous reservoirs is highly dependent on the flow and transport behavior during alternating injection and withdrawal cycles in the reservoir, which is governed by complex pore-scale processes [9,13,14]. Among the major mechanisms influencing UHS efficiency, residual trapping plays a critical role and is considered a significant source of hydrogen loss [14,15]. This is specially due to the fact that for UHS, hydrogen has to be trapped only temporarily and become mobile when extracted [16]. Residual trapping, however, is a mechanism that permanently traps hydrogen molecules in the subsurface microchannels. As such, residual trapping of hydrogen needs to be extensively investigated and properly managed in field-scale operations. Note that experimental studies have reported residually-trapped hydrogen saturation values as high as 44%, underscoring the importance of investigating its value upfront for proper site selection and effective operation [17–23].

Residual trapping, or capillary trapping, is defined as the fraction of hydrogen fluid that becomes immobile as disconnected volumes within the brine-saturated porous channels. The trapping is influenced by the pore geometry and the fluid-fluid and solid-fluid interactions [24], and can occur when capillary forces dominate over the other acting mobilizing forces, such as buoyancy, inertia, and viscous forces [25]. The two main capillary trapping mechanisms are bypassing trapping and snap-off [26,27]. Bypass trapping can be studied using the pore doublet model, i.e., a bifurcating channel splitting geometry [28–30]. This bifurcating geometrical structure consists of two channels with different channel widths splitting from a main flowing stream. It is specially used as a conceptualized model of the pore structure for the interpretation of the bypassing trapping mechanism, when non-wetting phase is displaced by the wetting phase [31,32]. Although conceptualized, the pore doublet model is used to gain deep understanding of the actual flow paths within complex pore networks, specially when channel splitting with sharp corners occurs. It can also serve as a building block for a larger network of channels, when scaled up into forming a microfluidic-type structured channelized system [33]. Recently, significant analytical and numerical advances have been made

* Corresponding author.
E-mail address: wangyuhang17@cug.edu.cn (Y. Wang).

https://doi.org/10.1016/j.ijhydene.2025.151274
Received 13 February 2025; Received in revised form 22 August 2025; Accepted 27 August 2025
Available online 18 September 2025

in understanding the pore doublet model, including the development of an analytical solution describing immiscible displacement dynamics [34]. In addition, Gu et al. [35] established a mathematical model and conducted numerical simulations to characterize the imbibition preference within the pore doublet. The pore doublet model has been extensively used in both experimental and analytical studies to investigate oil entrapment [26,28–30,36,37]. However, it has not yet been applied to the H_2/brine system, which exhibits significantly different fluid properties.

Residual trapping can be studied experimentally using core flood experiments [17,32,38–40,40] and micromodels [32,41,42]. However, these experiments can be challenging, time-consuming, and expensive and can only be carried out at limited conditions and with a limited number of samples [43–45]. Alternatively, numerical pore-scale simulations can be used to predict and understand trapping [38,46–51].

There are two main types of pore-scale simulations: Pore-Network Modeling (PNM) and fully-resolved simulations computational fluid dynamics (CFD) approach. In PNM, simulations are carried out using extensively simplified representations extracted from rock samples [9]. Pore volumes are represented as interconnected pores connected through throats. In fully-resolved CFD simulations, the pore structures are represented more explicitly, from either experimental characterization or numerical reconstruction, using what is referred to as digital rock technology [52]. Commonly employed CFD methods include the lattice Boltzmann method (LBM) [53], Level-Set method [54], and the Volume of Fluid (VoF) method [55].

LBM simulates the movement of an ensemble of particles on a lattice using the Boltzmann equation [45]. More traditional CFD methods are based on Navier–Stokes equations and use methods such as the VoF or the Level-Set method for interface tracking. Due to its good mass conservation properties and sharp interface representation, the VoF approach has been used in the literature [45,56]. However, LBM presents several notable advantages. One of its key strengths is its suitability for simulating flow in porous media, as it effectively handles complex geometries and boundary conditions with a relatively simple approach. Furthermore, LBM is amenable for parallel processing, enhancing its domain size relevance to what is expected to be a representative elementry volume in porous media systems [57–60].

In the context of UHS, various experimental and numerical studies at the core- and/or pore-scale have investigated residual trapping mechanisms and flow efficiency [9,16–23,61–65]. However, a limited number of studies have systematically focused on the underlying processes of residual trapping, specifically examining the physical and geometrical conditions that facilitate residual trapping in UHS scenarios. Similar as more structured micro-channel geometries [33], Lysyy et al. [21,63] also used microfluidics to study the displacement and trapping mechanisms of hydrogen in an aquifer storage scenario. Trapping by bypassing was one of the observed trapping mechanisms within their experiments. Wang et al. [52] conducted pore-scale simulations through the VoF method, to analyze hydrogen transport within a pore network representative under varying wetting conditions. They reported that, as expected, increasing hydrogen wettability is unfavorable for the extraction process. Similarly, Bagheri et al. [66] employed the VoF method in pore-scale simulations, to investigate the effect of flow regime, compressibility, and hysteresis on flow pattern, trapping mechanisms, and efficiency of hydrogen storage and found that lower flow rates favor capillary trapping through snap-off. Lastly, Yu et al. [25] reported the only study systematically focussing on the influence of pore geometry on trapping, a study that was also investigated in PNM on more simplified geometries [9]. They conducted pore-scale simulations through the VoF method to investigate the effects of pore geometry and injection rate on trapping via dead-end bypassing. They reported that higher injection rates cause more trapping by this mechanism. However, studies investigating other pore geometries than dead-end pores and their effect on trapping relevant to UHS are currently missing in the literature.

The objective of this study is to systematically investigate how physical and geometrical conditions influence the underlying trapping mechanisms in the context of UHS. Specifically, for bifurcating geometries, we examine the impact of (a) channel width ratio, (b) pore shape, (c) capillary number and flow velocity, and (d) fluid properties, through a comparison of the trapping behavior of H_2 with that of CH_4 and CO_2, on residual trapping by bypassing. To achieve this, we perform pore-scale simulations using our in-house developed lattice Boltzmann method, exploring various geometries. These geometries are chosen to conceptualize the splitting of streamlines, with and without sharp corners, into separate channels with various width aspect ratios. This fundamental study allows to identify what mechanism is driving hydrogen trapping in porous media with a wide range of channel widths and sharp corners. Specially we aim to analyze if those trapped hydrogen volumes can be mobilized by changing the flow rate, i.e., capillary number. What comes next indeed reveals the strength of LBM in allowing us to identify the process that leads to entrapment of hydrogen in bifurcating situations, and revealing in what way this can also help for better site selection based on the rock channel width distribution.

The structure of this paper is as follows: Section 2 outlines the methodology, including the governing equations and simulation methods. Section 3 describes the simulation setup, fluid properties, and pore geometries. In Section 4 we present a theoretical analysis, and in Section 5, we present the simulation results, and their application to underground hydrogen storage. Finally, the key findings are summarized in Section 6.

2. Methodology

2.1. Lattice Boltzmann method for immiscible two-phase flow

In this work, an immiscible two-phase color gradient LBM model [67–69] is developed. Two immiscible fluids are described by two sets of distribution functions f_α^R and f_α^B, where the two fluids are marked as red and blue phases. The total distribution function is defined as $f_\alpha = f_\alpha^R + f_\alpha^B$, which undergoes the collision step of

$$f_\alpha^*(\mathbf{x},t) = f_\alpha(\mathbf{x},t) + \Omega_\alpha(\mathbf{x},t) + \bar{F}_\alpha(\mathbf{x},t), \tag{1}$$

where $f_\alpha(\mathbf{x},t)$ is the total distribution function along α-direction at time t and position vector $\mathbf{x}$, f_i^* is the post-collision distribution function, Ω_α is the collision operator, and $\bar{F}_\alpha$ is the forcing term. To enhance the numerical stability, the multiple–relaxation–time (MRT) [70–73] scheme is used, and the collision operator reads

$$\Omega_\alpha(\mathbf{x},t) = -\left(\mathbf{M}^{-1}\mathbf{S}\mathbf{M}\right)_{\alpha\beta}\left(f_\beta(\mathbf{x},t) - f_\beta^{eq}(\mathbf{x},t)\right). \tag{2}$$

The transformation matrix $\mathbf{M}$ maps the distribution functions and their equilibrium ones onto the moment space, that is, $\mathbf{m} = \mathbf{M}\mathbf{f}$, $\mathbf{m}^{eq} = \mathbf{M}\mathbf{f}^{eq}$, where $\mathbf{m}$ (and $\mathbf{m}^{eq}$) denote the vector of macroscopic moments, specifically defined as:

$$\mathbf{m} = \left(\rho,\ e,\ \varepsilon,\ j_x,\ q_x,\ j_y,\ q_y,\ p_{xx},\ p_{xy}\right)^T, \tag{3}$$

where ρ is the density, e is the internal energy, ε is the square of internal energy, j_x and j_y are the momentum components in the x and y directions, respectively, q_x and q_y are the energy fluxes, and p_{xx} and p_{xy} represent the diagonal and off-diagonal components of the stress tensor. The transformation matrix $\mathbf{M}$ is explicitly given by

$$\mathbf{M} = \begin{pmatrix} 1 & 1 & 1 & 1 & 1 & 1 & 1 & 1 & 1 \\ -4 & -1 & -1 & -1 & -1 & 2 & 2 & 2 & 2 \\ 4 & -2 & -2 & -2 & -2 & 1 & 1 & 1 & 1 \\ 0 & 1 & 0 & -1 & 0 & 1 & -1 & -1 & 1 \\ 0 & -2 & 0 & 2 & 0 & 1 & -1 & -1 & 1 \\ 0 & 0 & 1 & 0 & -1 & 1 & 1 & -1 & -1 \\ 0 & 0 & -2 & 0 & 2 & 1 & 1 & -1 & -1 \\ 0 & 1 & -1 & 1 & -1 & 0 & 0 & 0 & 0 \\ 0 & 0 & 0 & 0 & 0 & 1 & -1 & 1 & -1 \end{pmatrix}. \tag{4}$$

The MRT operator allows each moment to relax at its own rate, with the relaxation rates stored in a diagonal matrix given by

$$S = \mathrm{diag}(s_0, s_1, s_2, s_3, s_4, s_5, s_6, s_7, s_8), \tag{5}$$

where the s_α denote the relaxation time for the αth moment in Eq. (5), in which s_{0-6} are constants and the values are followed the work of Xu et al. [68], specifically, $s_0 = 1$, $s_1 = 1.64$, $s_2 = 1.54$, $s_3 = 1$, $s_4 = s_6 = 1.9$, $s_5 = 1$; the parameter s_7 and s_8 are equal to $\frac{1}{\tau}$, where τ is the relaxation time that related to the kinematic viscosity ν, i.e.,

$$\nu = (\tau - 0.5)c_s^2 \delta t. \tag{6}$$

Here, c_s is the lattice sound speed in the D2Q9 model, defined as $c_s = c/\sqrt{3}$ with $c = \delta x/\delta t$. In this study, both δx and δt are set to unity. To account for the viscosity difference of the two phases, a harmonic mean is used to determine the viscosity of the fluid mixture [67], i.e.,

$$\frac{1}{\nu} = \frac{1+\rho^N}{2\nu_R} + \frac{1-\rho^N}{2\nu_B}, \tag{7}$$

where ν_R and ν_B are the kinematic viscosity of the fluids, and ρ^N is the phase field and is defined as

$$\rho^N(\mathbf{x}, t) = \frac{\rho_R(\mathbf{x}, t) - \rho_B(\mathbf{x}, t)}{\rho_R(\mathbf{x}, t) + \rho_B(\mathbf{x}, t)}. \tag{8}$$

f_α^{eq} is the discrete equilibrium Maxwellian distribution function expressed by

$$f_\alpha^{eq} = \rho\omega_\alpha \left[1 + \frac{\mathbf{e}_\alpha \cdot \mathbf{u}}{c_s^2} + \frac{(\mathbf{e}_\alpha \cdot \mathbf{u})^2}{2c_s^4} - \frac{\mathbf{u}^2}{2c_s^2}\right], \tag{9}$$

where $\rho = \rho_R + \rho_B$ is the total density, and ρ_R and ρ_B are the densities of red and blue fluids, respectively, $\mathbf{u}$ is the velocity of the fluid, $\mathbf{e}_\alpha$ is a vector of discrete velocities, c_s is the speed of sound, ω_α is the weighting factor. Here the two-dimensional nine-velocity (D2Q9) model is used, with the discrete velocities given by $\mathbf{e_0} = (0,0)$, $\mathbf{e_1} = -\mathbf{e_3} = (c,0)$, $\mathbf{e_2} = -\mathbf{e_4} = (0,c)$, $\mathbf{e_5} = -\mathbf{e_7} = (c,c)$, and $\mathbf{e_6} = -\mathbf{e_8} = (-c,c)$, where $c = \delta x/\delta t = \sqrt{3c_s^2}$, δx and δt are lattice spacing and time step, which are defined as unity; the weighting factor ω_α is given by $\omega_0 = 4/9$, $\omega_{1-4} = 1/9$, and $\omega_{5-8} = 1/36$.

The forcing term $\bar{F}_\alpha$ generates the interfacial tension between phases. In MRT scheme [74], the forcing term, first proposed by Guo et al. [75], is expressed as

$$\bar{\mathbf{F}} = \mathbf{M}^{-1}\left(\mathbf{I} - \frac{1}{2}\mathbf{S}\right)\mathbf{M}\tilde{\mathbf{F}}, \tag{10}$$

where $\mathbf{I}$ is a 9×9 unit matrix, $\mathbf{M}$ is the transformation matrix defined by Eq. (4) and $\tilde{\mathbf{F}}$ is given by

$$\tilde{F}_\alpha = \omega_\alpha\left[\frac{\mathbf{e}_\alpha - \mathbf{u}}{c_s^2} + \frac{(\mathbf{e}_\alpha \cdot \mathbf{u})\mathbf{e}_\alpha}{c_s^4}\right] \cdot \mathbf{F_s}\delta t, \tag{11}$$

where $\mathbf{F_s}$ is the body force that produces the local stress jump across the interface. Based on the continuum surface force (CSF) model of Brackbill et al. [76], the body force can be expressed as [77]

$$\mathbf{F_s} = -\frac{1}{2}\sigma\kappa\nabla\rho^N, \tag{12}$$

where σ is the interfacial tension, and κ is the local interface curvature, which is calculated by

$$\kappa = -\nabla_s \cdot \mathbf{n} = -(\mathbf{I} - \mathbf{nn}) \cdot \nabla \cdot \mathbf{n}. \tag{13}$$

Here, $\mathbf{n}$ is the unit normal vector defined as $\mathbf{n} = -\frac{\nabla\rho^N}{|\nabla\rho^N|}$. The local velocity takes the form as in

$$\rho\mathbf{u}(\mathbf{x}, t) = \sum_\alpha e_\alpha f_\alpha(\mathbf{x}, t) + \frac{\delta t}{2}\mathbf{F_s}(\mathbf{x}, t), \tag{14}$$

to incorporate the spatially varying body force [75]. In order to minimize the discretization errors, the nine-point compact finite-difference stencil is used in calculating the partial derivatives of the normal vector and the interface curvature.

To promote phase segregation and maintain a reasonable interface, the recoloring algorithm proposed by Latva-Kokko and Rothman [78] is adapted, the recolored distribution function of the fluids, f_α^{R**} and f_α^{B**}, are

$$\begin{aligned} f_\alpha^{R**} &= \frac{\rho_R}{\rho} f_\alpha^*(\mathbf{x}, t) + \beta\frac{\rho_R\rho_B}{\rho}\omega_\alpha \cos(\varphi_\alpha)|\mathbf{e_\alpha}|, \\ f_\alpha^{B**} &= \frac{\rho_B}{\rho} f_\alpha^*(\mathbf{x}, t) - \beta\frac{\rho_R\rho_B}{\rho}\omega_\alpha \cos(\varphi_\alpha)|\mathbf{e_\alpha}|, \end{aligned} \tag{15}$$

where β is the segregation parameter and is free to adjust, in this work, it is set to be 0.7, ϕ_α is the angle between the phase field gradient $\nabla\rho^N$ and the lattice vector $\mathbf{e}_\alpha$, defined by

$$\cos(\varphi_\alpha) = \frac{\mathbf{e_\alpha} \cdot \nabla\rho^N}{|\mathbf{e_\alpha}||\nabla\rho^N|}. \tag{16}$$

After the recoloring step, the distribution functions of red and blue phases propagate to the neighboring lattice nodes, known as propagation or streaming step:

$$\begin{aligned} f_\alpha^R(\mathbf{x} + \mathbf{e_\alpha}\delta t, t + \Delta t) &= f_\alpha^{R**}(\mathbf{x}, t), \\ f_\alpha^B(\mathbf{x} + \mathbf{e_\alpha}\delta t, t + \Delta t) &= f_\alpha^{B**}(\mathbf{x}, t). \end{aligned} \tag{17}$$

The post-propagation distribution functions are then used to obtain the local density of both fluids by $\rho_R = \sum_\alpha f_\alpha^R$ and $\rho_B = \sum_\alpha f_\alpha^B$. Eqs. (1)–(17) together define the complete evolution process, consisting of collision (Eqs. (1)–(2) and (10)), recoloring (Eq. (15)), and propagation/streaming (Eq. (17)).

2.2. Wetting boundary condition

In this work, the wetting boundary condition is imposed to achieve the prescribed contact angle θ at the solid surface, following the approach of Xu et al. [68]. The main steps are as follows: (1) estimate the ρ^N at the boundary solid nodes, (2) evaluate the color gradient $\Delta\rho^{N*}$ in boundary fluid nodes using the estimated ρ^N, and (3) correct the color gradient so that the local contact angle matches the desired value.

First, for each boundary solid node $x \in C_{S_B}$, the ρ^N is estimated by a weighted average of the neighboring fluid nodes, i.e.,

$$\rho^N(x) = \frac{\sum_{\alpha,\, x+\mathbf{e}_\alpha\delta t \in C_{F_B}} \omega_\alpha\, \rho^N(x + \mathbf{e}_\alpha)}{\sum_{\alpha,\, x+\mathbf{e}_\alpha \in C_{F_B}} \omega_\alpha}, \qquad x \in C_{S_B} \tag{18}$$

where C_{F_B} is the set of fluid nodes at the solid-fluid interface, C_{S_B} is the set of boundary solid nodes, ω_α are the weight coefficients, and $\mathbf{e}_\alpha$ are the discrete lattice velocities. The color gradient $\Delta\rho^{N*}$ at each fluid node near the boundary is then computed through nine-point compact finite-difference stencil, which needs to be modified to achieve the desired contact angle.

Next, the orientation of $\Delta\rho^{N*}$ in C_{F_B} is calculated as

$$\mathbf{n}^* = \frac{\Delta\rho^{N*}}{|\Delta\rho^{N*}|}. \tag{19}$$

In two dimensions, there are two possible candidate interface normal vectors at the contact line, $\mathbf{n}_1$ and $\mathbf{n}_2$ corresponding to the prescribed contact angle θ, which can be obtained by rotating the unit normal vector of the solid surface $\mathbf{n}_s = (n_{s,x}, n_{s,y})$ by θ in the positive and negative senses, i.e.,

$$\begin{aligned} \mathbf{n}_1 &= (n_{s,x}\cos\theta - n_{s,y}\sin\theta,\ \ n_{s,y}\cos\theta + n_{s,x}\sin\theta), \\ \mathbf{n}_2 &= (n_{s,x}\cos\theta + n_{s,y}\sin\theta,\ \ n_{s,y}\cos\theta - n_{s,x}\sin\theta). \end{aligned} \tag{20}$$

The correct unit normal vectors for the color gradient in C_{F_B} are selected by comparing the Euclidean distances to $\mathbf{n}^*$, i.e.,

$$\begin{aligned} D_1 &= |\mathbf{n}^* - \mathbf{n}_1| \\ D_2 &= |\mathbf{n}^* - \mathbf{n}_2|, \end{aligned} \tag{21}$$

The unit normal vector is then selected as

$$\mathbf{n} = \begin{cases} \mathbf{n}_1, & D_1 < D_2 \\ \mathbf{n}_2, & D_1 > D_2 \\ \mathbf{n}_s, & D_1 = D_2 \end{cases} \tag{22}$$

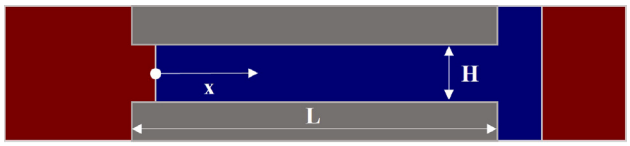

Fig. 1. Schematic of capillary intrusion.

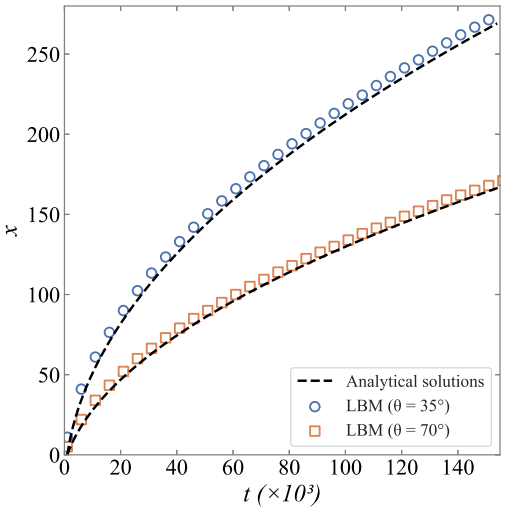

Fig. 2. Capillary intrusion tests: comparison between LBM simulations and theoretical predictions.

Finally, the color gradient vector at the boundary is modified as

$$\Delta\rho^N = |\Delta\rho^{N*}|\,\mathbf{n}, \tag{23}$$

ensuring that the local interface orientation matches the desired contact angle. This algorithm provides robust and accurate wetting boundary conditions for arbitrary contact angles and complex geometries, and is effective for two-phase lattice Boltzmann simulations in porous media.

The above color-gradient LBM was programmed in MATLAB, with the computational efficiency enhanced through parallel computing on the graphics processing unit (GPU), utilizing MATLAB's built-in functions (i.e. *conv2* for calculating the partial derivatives and *pagefun* for three-dimensional matrix operations). The simulations in this work were performed using the RTX 4090 GPU on workstations.

2.3. Capillary intrusion validation

To verify the developed model, the capillary intrusion test is performed. As sketched in Fig. 1, the simulation domain is a 2D capillary tube placed horizontally: The wetting phase penetrates the tube that initially filled by the non-wetting phase. This imbibition process is determined by the balance between capillary and viscous forces of the fluids, which can be expressed as

$$\sigma\cos(\theta) = \frac{6}{H}\left[\mu_L x + \mu_V (L-x)\right]\frac{dx}{dt}, \tag{24}$$

where θ is the contact angle, L and H are the length and width of the capillary tube, respectively; x is the location of the interface, μ_L and μ_V are dynamic viscosities of liquid and vapor phases [67]. The domain is discretized into 600 × 15 lattice points with $L = 300$ and $H = 5$ for the capillary tube with periodic boundary conditions in the x direction. Here we take brine displacing H_2 as example, and the parameters used in the simulation is listed in Table 2, Periodic boundary conditions are imposed on the region occupied by fluid.

We consider two cases with the contact angle given by $\theta = 35°$ and $\theta = 70°$. Fig. 2 presents the comparisons between numerical simulations from LBM and the analytical predictions of Eq. (24). Good agreement was observed with capillary width H being 5, which was smaller than the smallest pore width in the following cases, ensuring that grid resolution is sufficient to capture the underlying dynamic processes.

3. Simulation setup and pore-scale characterization

3.1. Fluid properties

The physical properties of H_2, CH_4, and CO_2 are listed in Table 1. These properties represent the conditions of a temperature of 40 °C and a pressure of 11 MPa, corresponding to a reservoir at a depth of 1100 m, which is identified as the optimal depth for hydrogen storage [79]. For the brine, a molality of 2.0 mol NaCl/L was selected, and the corresponding properties were applied. The contact angles, which are similar for the three gases, were derived from experimental measurements [80–82]. All measurements were conducted in the same laboratory using the Captive Bubble method on sandstone samples, providing a consistent basis for comparison. To convert the physical properties into lattice units, fixed scaling parameters for length, mass, and time were applied, resulting in the values presented in Table 2.

The densities of both the gas and the brine were set to one, assuming negligible inertial forces in the system, consistent with low Reynolds numbers and laminar flow conditions [83]. This simplification excludes gravitational (buoyancy-driven) effects, which may become relevant in larger-scale systems, but were not the focus of this capillarity-driven trapping study [83,84]. The mass scaling factor was calculated based on the liquid density. In these simulations, dynamic viscosity ratios were used. Using dynamic viscosities ensures a realistic representation of the mobility of both the gas and the liquid phase.

3.2. Pore geometry

The primary pore geometry used in this study is the pore doublet model, shown in Fig. 3 (left). Although highly idealized compared to real pore networks, this geometry captures key aspects of preferential flow and multiphase displacement behavior in porous media [34,91]. Its simplicity allows for isolating the fundamental physical mechanisms governing trapping due to bypassing, which are relevant to more complex geological systems. The pore doublet model comprises an inlet channel that bifurcates into two parallel channels with different widths, d_1 and d_2, before merging into a single outlet channel. To investigate the effect of pore shape, a rounded version of the pore doublet model is also employed (Fig. 3 (right)). The rounded model has the same inlet width, d_1, as the rectangular pore doublet model, to maintain consistency. In all geometries d_1 is set as 15, and the corresponding d_2 is set based on the channel width ratio.

3.3. Simulation setup

The Zou–He type boundary conditions are adopted in this study [92,93], with a constant pressure prescribed at the inlet and a zero-pressure condition at the outlet. To achieve no-slip condition, the halfway bounce-back scheme [94,95] is applied at the solid walls. The inlet velocity caused by the set pressure gradient, is used to define the capillary number, which is defined as

$$Ca \equiv \frac{\mu_{gas}\cdot|V_{inlet}|}{\sigma}. \tag{25}$$

The investigated capillary numbers are in the range of 10^{-4}, which is relevant for the UHS systems [96]. At the start of the simulation, the system is fully saturated with brine, and a volume fraction of 100% gas is set at the left boundary. As the pressure gradient is applied, gas flows into the system from the left boundary, simulating the drainage process. During the drainage phase, no gas trapping is expected. However, this phase is included to establish a realistic initial phase distribution for the

Table 1
Physical units of H_2, CH_4, CO_2, and brine (2.0 mol NaCl/L) at T = 40 °C and P = 11 MPa. Values are taken based on the literature [80–82,85–90].

Property	Unit	H_2	CH_4	CO_2
Density gas, ρ_{gas}	kg/m^3	8.00	77.6	683
Density liquid, ρ_{brine}	kg/m^3	1066	1066	1066
Dynamic Viscosity gas, μ_{gas} ($\nu_{gas} \cdot \rho_{gas}$)	μPa s	9.47	14.3	54.1
Dynamic Viscosity liquid, μ_{brine} ($\nu_{brine} \cdot \rho_{brine}$)	μPa s	790	790	790
Viscosity ratio gas/brine M	–	0.012	0.018	0.068
Surface tension, σ	mN/m	66	58	39
Contact angle, θ	°	35	35	30

Table 2
Lattice units H_2, CH_4, CO_2, and brine, used in the numerical simulations, expressed in units of mass (M), length (T) and time (T).

Property	Unit	H_2	CH_4	CO_2
Density gas, ρ_{gas}	M/L^3	1	1	1
Density liquid, ρ_{brine}	M/L^3	1	1	1
Dynamic Viscosity gas, μ_{gas} ($\nu_{gas} \cdot \rho_{gas}$)	M/L T	0.0060	0.0091	0.034
Dynamic Viscosity liquid, μ_{brine} ($\nu_{brine} \cdot \rho_{brine}$)	M/L T	0.50	0.50	0.50
Viscosity ratio gas/brine M	–	0.012	0.018	0.068
Surface tension, σ	M/T^2	0.19	0.16	0.11
Contact angle, θ	°	35	35	30

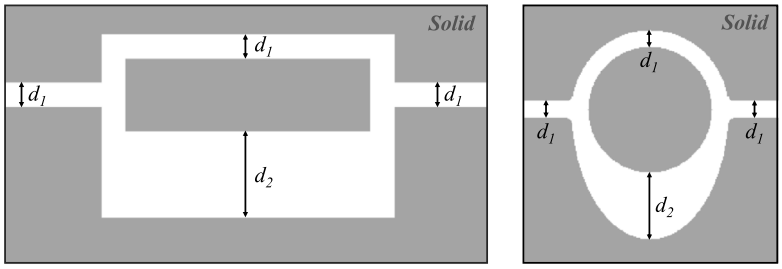

Fig. 3. Pore geometries used in this study: (left) Rectangular pore doublet model, (right) Rounded pore doublet model.

subsequent imbibition phase. Once the gas reaches the right boundary of the simulation box, the imposed pressure gradient is reversed and adjusted, resulting in the specific capillary number of the test (which are in the range of 10^{-4}). The volume fraction at the right boundary is then set to 100% brine, simulating brine injection from this boundary (imbibition). The simulation ends when no further changes in phase distribution occur.

3.4. Test cases

The goal of the simulations is to understand trapping due to bypassing in H_2/brine systems. More specifically, we aim to understand the impact of (a) channel width ratio, (b) pore shape, (c) capillary number and flow velocities, and (d) fluid properties, through a comparison of the trapping behavior of H_2 with that of CH_4 and CO_2.

A series of simulations have been carried out in which the channel width ratio (d_2/d_1) was varied in the rectangular pore doublet from 2.5 to 5.0. To investigate the influence of pore/grain shape, similar simulations were carried out using the rounded pore doublet with a channel width ratio from 4.0 to 6.0. To assess the role of fluid properties in trapping behavior, simulations are carried out for H_2 as well as for CH_4 and CO_2.

4. Theoretical analysis of the pore doublet model

To understand the outcome of our numerical simulations, we conduct a theoretical analysis of bypassing in the pore doublet model. The pore doublet model is a parallel arrangement of a small and large-diameter channel, and is used as an idealized model of a pore structure for the interpretation of trapping of the non-wetting phase by the displacing wetting fluid during immiscible displacement in permeable porous media [31,32]. A schematic pore doublet model is presented in Fig. 4.

The entrapment of oil, as a non-wetting fluid, has been studied extensively by various researchers [28,29,37,97]. Their analyses indicate that, under specific conditions, the fluid interface in the small capillary at point A will progress towards point B, while the interface in the larger capillary remains stationary. This behavior is attributed to the higher capillary pressure in the narrow channel, which makes it the preferential flow path. However, once the interface in the larger capillary reaches point B, it may also become stationary. This occurs because further advancement requires the expansion of the interface area, which affects the capillary pressure.

In some cases, the interface expands until it contacts the opposite wall of the channel, leading to a snap-off event. When this happens, the non-wetting fluid becomes trapped in the larger capillary. Conversely, under different conditions, the interface in the smaller capillary may also advance towards point B, preventing fluid trapping in the system.

4.1. Pressure balance and trapping conditions

The pressure drop across each channel is the sum of the capillary pressure and the viscous pressure drop [28]. Because the two channels are interconnected at both ends, the overall pressure difference in the

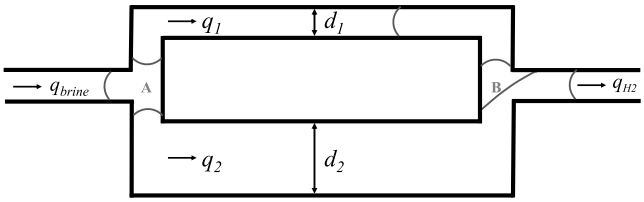

Fig. 4. Pore doublet model representation of imbibition. (Inspired by Chatzis and Dullien [32]).

two channels is identical [30,32]. During imbibition, as the wetting fluid enters the system, capillary pressure enhances the flow velocity, while the viscous forces act to resist the flow. Consequently, capillary forces and viscous forces operate in opposing directions. When the pressure gradients in the inlet and outlet channels are negligible, this equivalence approximates the overall pressure difference between the inlet and outlet:

$$P_{inlet} - P_{outlet} \approx P_{c_1} - \Delta P_1 = P_{c_2} - \Delta P_2, \tag{26}$$

where P_{inlet} and P_{outlet} denote the set pressures at the inlet and outlet, respectively. The terms P_{c_1} and P_{c_2} represent the capillary pressures in channels 1 and 2, and ΔP_1 and ΔP_2 correspond to the viscous pressure drops in channels 1 and 2, respectively.

The viscous pressure drop in each channel can be estimated by the Hagen–Poiseuille equation [37,97], i.e.,

$$\Delta P_j = \frac{128 q_j \mu l}{\pi d_j^4} \quad (j = 1, 2), \tag{27}$$

where d_1 and d_2 are the diameters of the large and small capillaries, respectively, l is the length of the flow path in the doublet, and μ is the dynamic viscosity. Eq. (27) assumes cylindrical capillaries and laminar flow.

The magnitude of capillary pressure P_c can be estimated by the Young–Laplace equation:

$$P_{cj} \equiv \left(P_{nw} - P_w\right)_j = \frac{4\sigma \cos\theta}{d_j} \quad (j = 1, 2), \tag{28}$$

where σ is the interfacial tension, θ is contact angle, and the subscripts nw and w indicate the non-wetting and wetting phases, respectively.

Trapping of the non-wetting phase in the pore doublet model will occur during the imbibition phase when capillary forces dominate over viscous forces [32]. Various attempts have been made to predict the exact conditions at which snap-off occurs [31,32]. The entrapment of the non-wetting phase is despite the fluid properties, largely dependent on the exact pore geometry [32], and therefore general trapping criteria are challenging to find and there is no consensus reached in the literature. However, the impact of various factors can be predicted by comparing the relative importance of capillary forces to viscous forces. Although the simulations are conducted in 2D, Eqs. (27) and (28) are based on 3D theory. These 3D expressions are more commonly used in the literature and provide a better representation of realistic porous media behavior. Since our analysis focuses on relative trends rather than absolute magnitudes, applying the 3D form allows for more general and transferable insights. In addition, it serves as a check on whether the 2D simulations reproduce the qualitative behavior expected from 3D systems.

4.2. Impact of flow velocities, channel width ratio, channel geometry, and fluid properties

Eqs. (27) and (28) indicate that the capillary pressure within each channel is independent of the flow rate (q). In contrast, the viscous pressure drop increases with flow rate. Consequently, at higher flow rates, viscous forces become more dominant relative to capillary forces. Since higher flow rates require a greater overall pressure gradient, this corresponds to higher capillary numbers. Trapping is most likely to occur when capillary forces dominate over viscous forces. This condition is met at low flow rates, which correspond to lower pressure gradients and capillary numbers. Therefore, as the capillary number decreases, the probability of trapping increases.

Eq. (28) shows that capillary pressure increases as channel width decreases. As a result, very narrow channels exhibit significantly higher capillary pressures. When the width ratio between the larger and smaller channels is greater, the capillary pressure within the narrow channel becomes more dominant within the system, promoting flow through the narrow channel and causing bypassing of the larger channel. Consequently, a higher channel width ratio increases the likelihood of trapping at certain capillary numbers.

As illustrated in Fig. 4, trapping is highly influenced by local forces that determine whether a snap-off event occurs. At the junction where the two channels reconnect, there is always a localized resistance due to the expansion of the interfacial area. The exact geometry of this junction plays a critical role in determining whether trapping occurs. In wider and more rounded geometries, the interfacial area at the potential snap-off location is larger, which reduces the likelihood of snap-off. Conversely, in sharper or more constricted geometries, the interfacial area is smaller, increasing the probability of trapping.

Eqs. (27) and (28) show that fluid properties such as viscosity, interfacial tension, and contact angle influence the balance between viscous and capillary forces. Higher viscosity increases viscous forces, while higher interfacial tension and lower contact angle increase capillary forces. Based on the fluid properties in Table 1, CO_2 shows the strongest dominance of viscous forces over capillary forces due to its high viscosity and low interfacial tension and contact angle, followed by CH_4 and then H_2. As a result, at the imposed same pressure gradients or velocities, CO_2 is most likely to bypass and become trapped, followed by CH_4 and finally H_2. Increasing brine salinity affects both viscosity and interfacial tension. It leads to higher viscosity [87] and also higher interfacial tension [88], which suggests that both viscous and capillary forces may increase. Therefore, the impact is expected to be minimal.

The fluid properties used in this study correspond to conditions at 11 MPa and 40 °C. While fluid properties vary with pressure and temperature, particularly for gases, these variations are less pronounced for the liquid-phase brine. At greater depths, the viscosity and density of H_2 would increase slightly, reducing the viscosity and density contrast with brine. However, given the inherently low viscosity and density of H_2 compared to brine, these changes are expected to have a minimal impact on the trapping behavior in this study. The H_2-brine surface tension is not significantly dependent on pressure, and is expected to decrease with temperature [88], suggesting less pronounced capillary forces in deeper reservoirs. The contact angle is expected to be independent of pressure and temperature [80].

5. Results and discussion

Our results reveal the conditions under which trapping due to bypassing occurs within a pore doublet model. Specifically, we quantify the trapping percentage observed after a drainage-imbibition cycle in cases where trapping occurs, which is summarized in Fig. 6. The following sections provide a detailed discussion of our simulation results, offering a systematic understanding of the factors influencing trapping within the pore doublet model.

In Section 5.1, we examine the impact of capillary numbers, which correlate with flow velocities representing specific injection and production rates. Section 5.2 explores the impact of the channel width ratios and pore size distributions in various geometries. In addition, the influence of pore shape is also investigated and discussed in this section. In Section 5.3, we discuss the influence of fluid properties on trapping by comparing the behavior of H_2, CH_4, and CO_2.

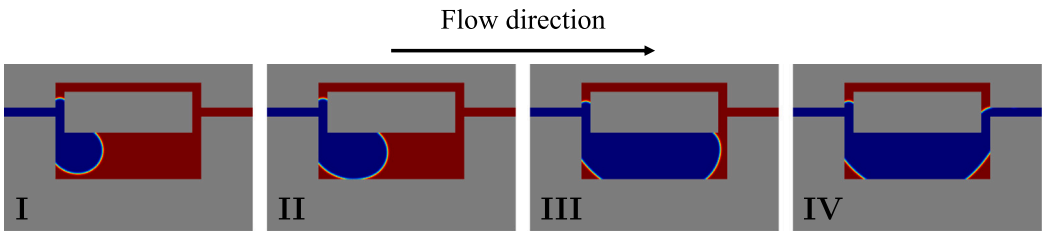

(a) Drainage test with flow from left to right.

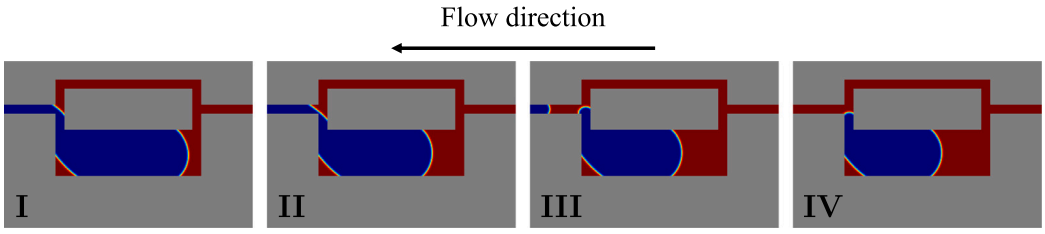

(b) Imbibition test with capillary number of 4.0×10^{-4} with flow from right to left.

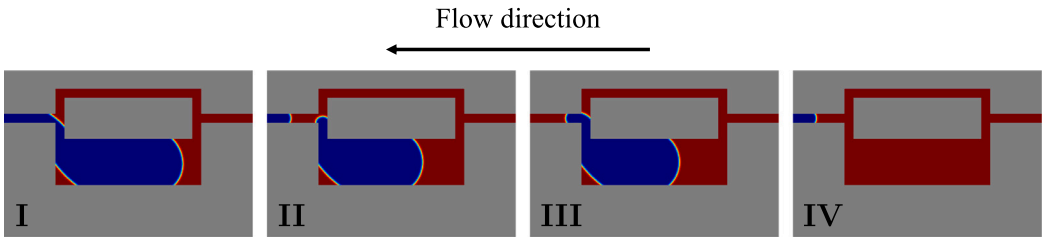

(c) Imbibition test with capillary number of 5.0×10^{-4} with flow from right to left.

Fig. 5. Frames from drainage (a) and imbibition (b and c) tests. Red represents brine and blue represents H_2. Trapping occurred during imbibition with capillary number 4.0×10^{-4} (b), while it did not occur for a higher capillary number of 5.0×10^{-4} (c). (For interpretation of the references to color in this figure legend, the reader is referred to the web version of this article.)

5.1. Impact of capillary number

Theoretical analysis predicts that larger capillary numbers, corresponding to higher flow velocities, result in a lower probability of trapping. Our results confirm this relationship. Fig. 5(a) illustrates the initial drainage phase for all tests, where the system is fully saturated with brine, and H_2 is injected from the left. As anticipated, H_2 preferentially flows through the larger channel due to both lower capillary and viscous resistance. During this phase, trapping of H_2 is not expected, so in the remainder of this section, the focus will be on the imbibition phase.

Once H_2 reaches the outlet, the flow is reversed to initiate the imbibition phase, during which brine is injected from the right with varying capillary numbers. Fig. 5(b) shows the imbibition phase of a test with a capillary number of 4.0×10^{-4}, showing brine flow through both channels initially. However, the smaller channel exhibits favorable conditions for flow due to the relatively large capillary pressure pulling the brine inward, eventually leading to snap-off in the third frame. Subsequently, brine flows exclusively through the smaller channel, leaving H_2 trapped in the larger channel (fourth frame).

Fig. 5(c) shows results for a higher capillary number (5.0×10^{-4}), where increased viscous forces decrease the influence of capillary forces. In this case, snap-off is observed in the second frame, but the detached bubble is mobilized again, and eventually, all H_2 is swept from the system.

Fig. 6 shows the trapping percentages for various tests using a range of capillary numbers for the imbibition phase. As anticipated, there is a certain threshold in capillary numbers for trapping to occur. This "threshold" or "critical capillary number" represents a sharp decrease

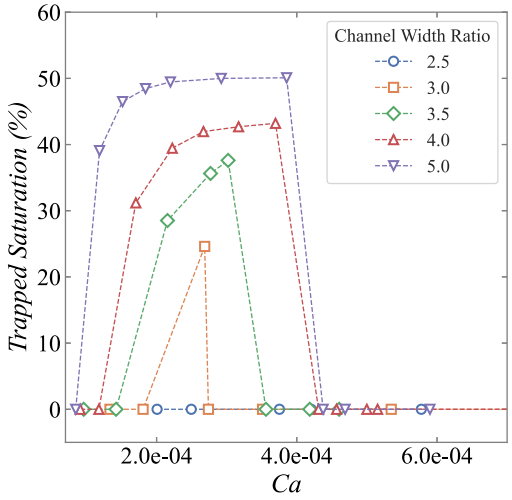

Fig. 6. Comparison of H_2 trapping percentages after imbibition for various channel width ratio's across capillary numbers in the rectangular pore doublet model.

in trapping percentage with increasing capillary numbers, due to the transition from dominating viscous forces to capillary forces. This sharp decrease in trapping has also been observed on the larger scale in both experiments and numerical simulations [36,98–101]. The exact threshold depends on the geometry of the system, which will be further

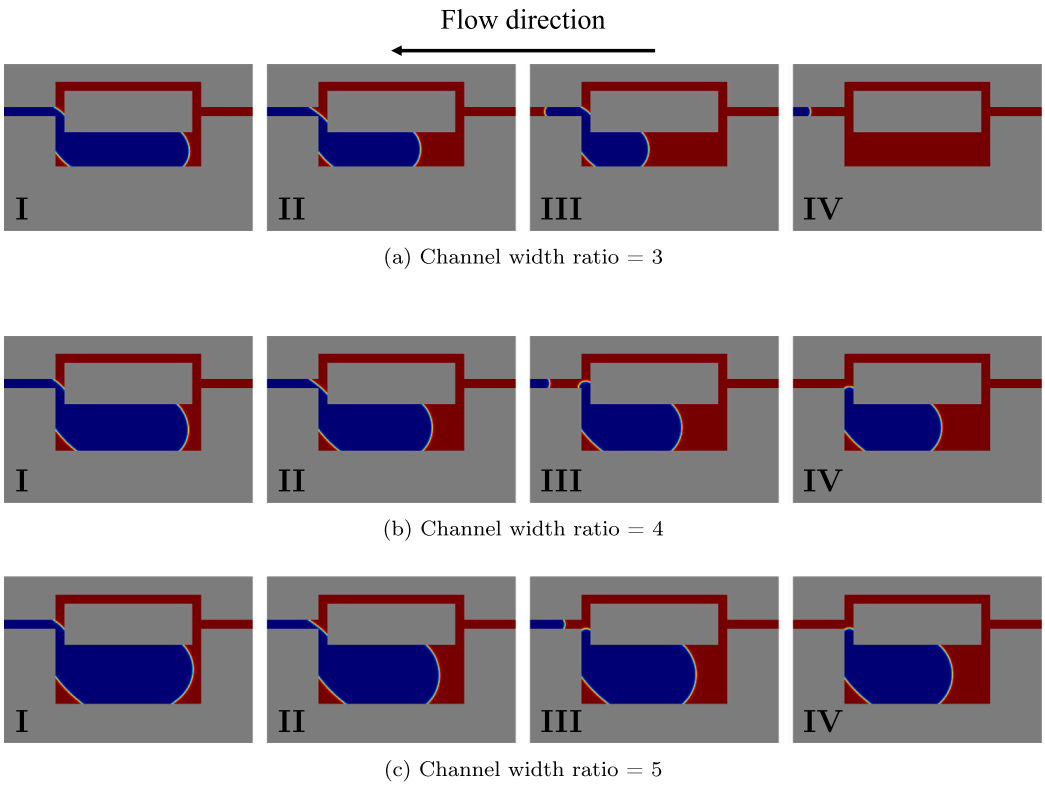

(a) Channel width ratio = 3

(b) Channel width ratio = 4

(c) Channel width ratio = 5

Fig. 7. Frames from imbibition tests with channel width ratios of 3 (a), 4 (b), and 5 (c) with capillary number of 4×10^{-4}. Red represents brine and blue represents H_2. The frames taken at the moment when (I) the wetting phase enters the large channel (II) snap-off is about to happen (III) snap-off just happened (IV) steady-state is reached. (For interpretation of the references to color in this figure legend, the reader is referred to the web version of this article.)

discussed in the next section. In some of the cases we can also observe a decrease in trapping percentage as capillary numbers decrease. This will also be further discussed in the next section.

5.2. Impact of channel width ratio and pore size distributions in various geometries

Fig. 7 illustrates four frames from three different test cases with channel width ratios of 3, 4, and 5, shown in panels (a), (b), and (c), respectively. All test cases shown in this figure were conducted at a similar capillary number of 4×10^{-4}. It can be observed that trapping did not occur in the test case where the channel width ratio was 3, whereas trapping was observed in the test cases with larger channel width ratios of 4 and 5.

These results align with theoretical predictions, which suggest that a larger difference in channel width enhances the dominance of capillary forces over viscous forces. This increased influence of capillary forces leads to the trapping phenomenon observed in cases with higher channel width ratios. Consistent with this observation, Fig. 6 demonstrates that larger channel width ratios correspond to a higher threshold for trapping.

Furthermore, larger width ratios result in higher trapping percentages. This can be attributed to the increased dominance of capillary forces in systems with greater channel width disparities. While trapping can still occur in cases with smaller channel width ratios, the flow of brine through the upper channel is slower relative to the flow in the larger channel compared to cases with larger ratios. In these instances with larger ratio, snap-off occurs more quickly and as a result, the brine does not advance as far in the lower channel, resulting in a higher trapping percentage.

Fig. 6 indicates that for smaller channel width ratios, trapping percentages decrease as capillary numbers drop below the trapping threshold. Interestingly, no trapping is observed for the lowest capillary numbers, which appears counterintuitive. To understand this behavior, it is essential to examine the geometry and the moment when snap-off nearly occurs, as illustrated in Fig. 8, this point in the simulation corresponds to point B in Fig. 4.

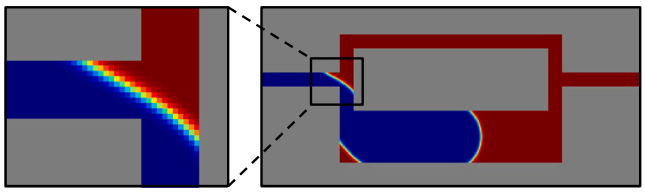

Fig. 8. Frame of the moment where snap-off nearly occurs, leading to trapping.

At low capillary numbers, capillary forces dominate, resulting in preferential flow through the upper channel. However, when the fluid interface reaches the junction where the two channels merge into the outlet channel (point B in Fig. 4), the interface temporarily widens as though the channel abruptly expands. This widening reduces the local capillary pressure, while the narrower channel still experiences relatively high viscous forces. Consequently, despite the general advantage of the upper channel, this temporary reduction in capillary pressure creates a local disadvantage, as also explained in the theoretical analysis (Section 4). When flow velocities are higher, the increased kinetic energy helps to overcome this local disadvantage, allowing snap-off to occur. Conversely, at very low velocities (low capillary numbers), this disadvantage significantly delays snap-off. In some cases, the delay is so pronounced that the flow through the lower, wider channel becomes dominant, and snap-off does not occur at all.

This analysis highlights the critical role of exact geometry in determining the trapping threshold. To further investigate, similar simulations were conducted using a rounded pore doublet model, as described

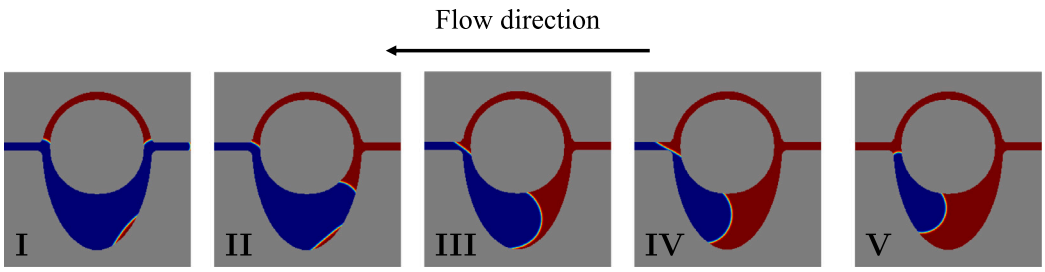

Fig. 9. Frames from imbibition test with the rounded pore doublet with a channel width ratio (d_2/d_1) of 5 and capillary number of 3.5×10^{-4}. Red represents brine and blue represents H_2. (For interpretation of the references to color in this figure legend, the reader is referred to the web version of this article.)

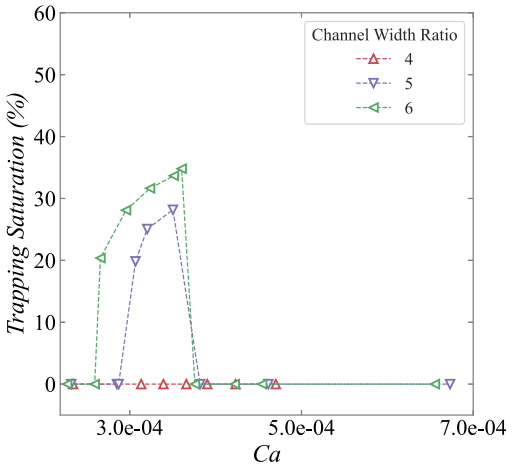

Fig. 10. Comparison of H_2 trapping percentages within the rounded pore doublet model for various channel width ratio's across capillary numbers.

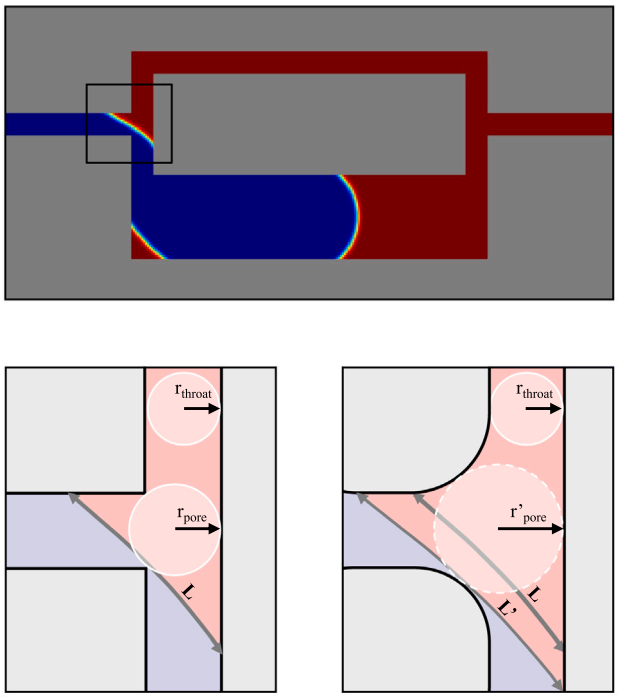

Fig. 11. Illustration of the influence of pore throat aspect ratio on capillary trapping. In the rectangular geometry (left), sharp transitions between throat and pore result in lower aspect ratios (r_{pore}/r_{throat}) and less reduced local capillary pressure, promoting trapping. In contrast, the rounded geometry (right) features smoother transitions and a higher aspect ratio (r'_{pore}/r_{throat}), as well as a lower capillary pressure due to the longer interface L', reducing the likelihood of trapping under comparable conditions.

in Fig. 3 (left), with varying channel width ratios. Trapping was also observed in this geometry under specific conditions, an example of which is presented in Fig. 9.

The results are summarized in Fig. 10. In this geometry, trapping occurs only for channel width ratios of 5 and higher, with trapping percentages ranging from 0% to 35%. When compared to the results obtained from the rectangular pore doublet model (Fig. 6), a similar trend can be observed. As the channel width ratio increases, both the trapping percentages and the capillary number thresholds for trapping increase. However, the absolute trapping percentages and thresholds are lower for the rounded pore doublet model at specific channel width ratios.

These findings suggest that the rectangular structure enhances trapping compared to the rounded structure, while maintaining the same general relationships between channel width ratio, trapping percentage, and capillary number thresholds. This difference can also be understood in terms of the pore throat aspect ratio, defined as the ratio between the wider junction area (acting as a pore) and the narrower connecting channels (throats), as illustrated in Fig. 11. In the rounded geometry, the pore radius is larger than in the rectangular geometry ($r'_{pore} > r_{pore}$), effectively increasing the aspect ratio. Consequently, the interface must extend further before reaching the opposite side of the channel ($L' > L$), which lowers the local capillary pressure. As a result, snap-off and the resulting trapping are delayed or less likely to occur. Overall, the smoother and more open junction in the rounded geometry contributes to reduced trapping under comparable conditions.

Our observations are consistent with the recent analytical work of Shan et al. [34], who derived an analytical solution for immiscible displacement in a pore doublet. They demonstrated that the displacement process is governed by a critical capillary number, which depends on both the viscosity ratio and the channel radius ratio. When the system operates below this critical number, preferential imbibition occurs in the narrow channel, leading to trapping in the wider channel. At higher capillary numbers, viscous forces dominate and trapping is reduced. These theoretical predictions align well with our LBM results, which show that increasing the channel width ratio promotes bypassing and enhances trapping at low capillary numbers.

5.3. Impact of gas type

Fig. 12 presents frames from an imbibition test conducted at a capillary number of 4×10^{-4} and a channel width ratio of 4. The top row (a) shows frames from a test using H_2 properties for the non-wetting phase, with corresponding tests for CH_4 and CO_2 properties shown in panels (b) and (c), respectively. For this capillary number, trapping is observed for both H_2 and CH_4, while for CO_2 no trapping is observed. It can be observed that the behavior of H_2 and CH_4 is quite similar, and similar gas saturations remain trapped, which is already expected due to their similar thermophysical properties.

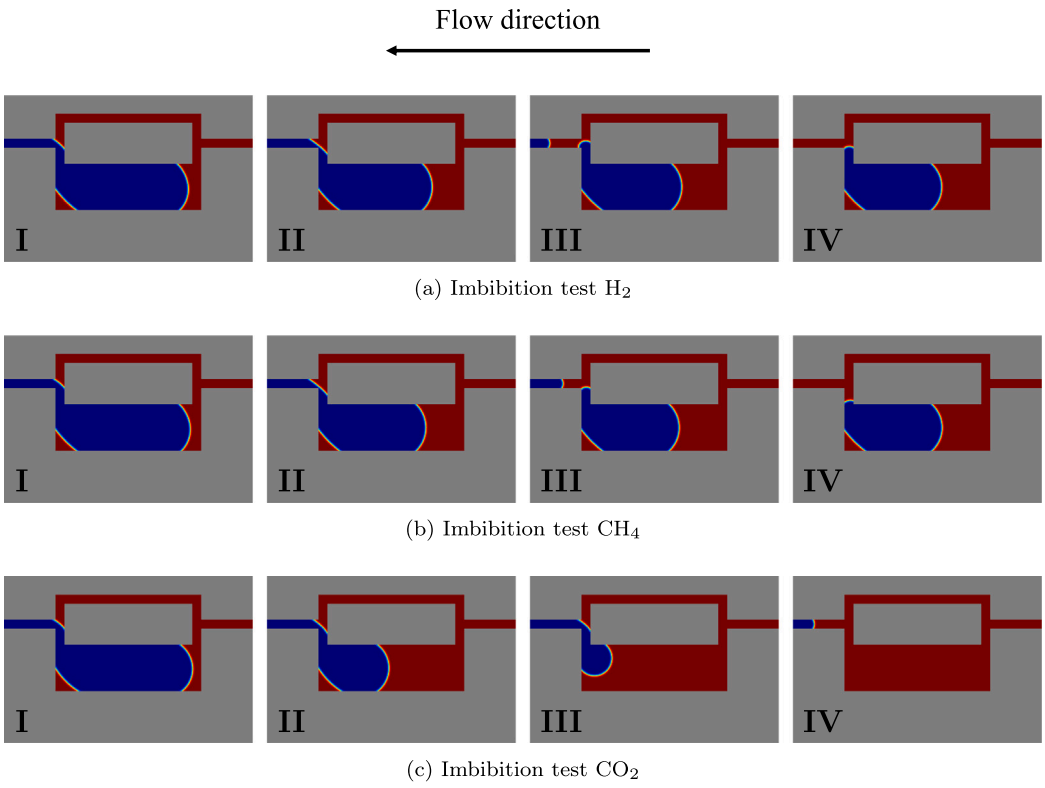

Fig. 12. Frames from imbibition tests with H_2 (a), CH_4 (b), and CO_2 (c) with capillary number of 4×10^{-4}. Red represents brine and blue represents the gas phase. Frames are taken at the moment when (I) the wetting phase enters the large channel (II) snap-off is about to happen (III) snap-off just happened (IV) steady-state is reached. (For interpretation of the references to color in this figure legend, the reader is referred to the web version of this article.)

Fig. 13 shows the trapped saturations of H_2, CH_4, and CO_2 as a function of the capillary number. Among the three gases, H_2 exhibits the lowest capillary trapping threshold at 3.8×10^{-4}, followed by CH_4 at 4.1×10^{-4}, and CO_2 with a significantly higher threshold of 1.1×10^{-3}. The capillary number represents the ratio of viscous to capillary forces, which governs trapping through bypassing. However, it does not include the viscosity ratio between the gas and liquid phases. Our results show a clear influence of viscosity ratio on the trapping behavior. H_2 has the lowest gas-to-liquid viscosity ratio (0.012), CH_4 is slightly higher (0.018), and CO_2 is much higher (0.067), which aligns with the observed trapping thresholds. Since only the gas viscosity is used in our capillary number definition, and not the liquid viscosity, the effect of gas viscosity is overestimated in systems that are not fully gas-saturated. This results in lower apparent capillary thresholds for gases with lower viscosities.

Based on our results, H_2 and CH_4 exhibit similar trapping behavior. The capillary number alone does not fully capture the dynamics of two-phase flow, particularly when it includes only the viscosity of the gas phase. However, examining the inlet velocities V_{inlet} at which capillary trapping begins reveals that H_2 and CH_4 reach their trapping thresholds at higher velocities than CO_2. This suggests that, at comparable production rates, H_2 and CH_4 are more likely to be trapped due to bypassing, while CO_2 may remain more mobile under the same conditions due to its higher viscosity and therefore stronger viscous forces.

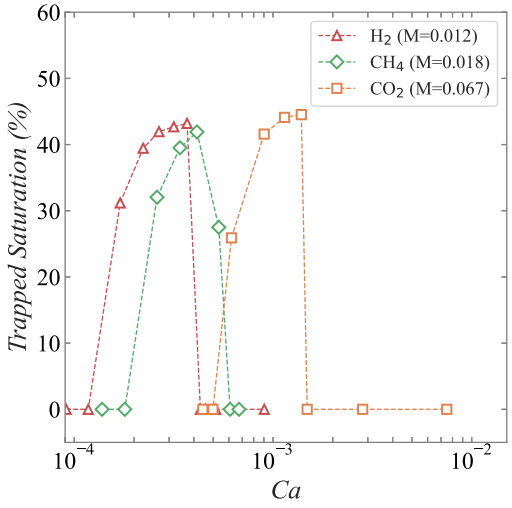

Fig. 13. Comparison of trapping percentages for H_2, CO_2, and CH_4 across capillary numbers. A channel width ratio of 4, and the rectangular pore doublet were used in the numerical simulations.

5.4. Application to UHS systems

The findings of this study are relevant to underground hydrogen storage (UHS), where understanding and predicting trapping mechanisms is critical for optimizing storage efficiency and minimizing losses. While the geometries used in this study do not replicate real pore structures, simplified geometries were intentionally chosen to develop a fundamental understanding of capillary trapping caused by bypassing and to identify trends applicable to UHS.

Our results show that trapping efficiency is strongly influenced by the distribution of pore sizes. A higher channel width ratio, representing a broader pore size distribution in rock formations, significantly enhances trapping due to bypassing. This indicates that reservoirs with wider pore size distributions are likely to immobilize greater amounts

of hydrogen through capillary trapping. This will reduce overall efficiency, particularly during initial storage cycles, as some of the injected hydrogen may remain trapped and unrecoverable.

Additionally, pore geometry was found to have a significant influence on the extent of trapping. Trapping due to bypassing is less likely to occur in rounded pores compared to rectangular shapes with sharp corners, and the trapping percentages are correspondingly lower in geometries with rounded corners. This suggests that selecting a rock type with well-rounded grains, rather than angular grains with sharp edges and corners, could reduce trapping and improve storage efficiency.

The observed dependence of trapping on the capillary number highlights the critical role of flow conditions during withdrawal phases. Lower capillary numbers, associated with slower flow rates, were found to increase trapping within our pore geometry. Extrapolating this to larger UHS systems suggests that producing H_2 from the reservoir at higher flow rates would enhance efficiency by reducing the amount of residually trapped H_2.

Interestingly, the findings of Yu et al. [25] suggest that higher flow rates can promote trapping due to dead-end bypassing. However, the broader consensus at the core scale indicates that the total amount of capillary-trapped non-wetting phase after imbibition generally increases with decreasing capillary number [100]. This conclusion is supported by both numerical and experimental studies [36,98,99,101]. In the context of H_2, it is also observed in core flood experiments that injection of brine at higher flow rates reduced capillary trapping and increased H_2 recovery [65]. These results reinforce our conclusion that higher production rates for H_2 extraction are likely to reduce residual trapping percentages.

The geometries used in our study were intentionally simplified to investigate the fundamental processes of capillary trapping due to bypassing. This phenomenon is inherently complex and highly sensitive to specific pore geometries and flow regimes. While these simplified geometries are essential for understanding the mechanisms driving certain processes observed at larger scales, they are not directly representative of real-world UHS scenarios.

To address these limitations, future research should focus on integrating these pore-scale insights into larger-scale reservoir models or conducting more realistic pore-scale simulations. Such efforts will facilitate more accurate predictions of trapping behavior and storage efficiency under conditions that better reflect practical applications. Moreover, trapping due to bypassing represents only one of the two primary capillary trapping mechanisms. To develop a more comprehensive understanding of the total amount of capillary trapping, future studies should also investigate the dynamics of trapping caused by snap-off. This dual focus will provide a more complete perspective on the factors influencing trapping efficiency in subsurface systems.

In addition to UHS systems, the trapping behavior analyzed in this study may also have implications for natural hydrogen extraction and in situ hydrogen generation [102,103]. These promising technologies involve subsurface environments in which hydrogen may occupy different pore structures and regions compared to UHS, potentially making recovery more challenging. Understanding the mechanisms of bypassing and trapping can therefore provide valuable insight into efficiency and recoverability in such settings.

6. Conclusions

This study aimed to provide a deeper understanding of how pore geometry and flow rate influence the residual trapping of H_2 by bypassing and to connect these mechanisms to the pore size distributions of rocks. Pore-scale simulations were conducted using the lattice Boltzmann method (LBM) across a variety of geometries, including the pore doublet model, to investigate the impact of (a) channel width ratio, (b) pore shape, (c) capillary number and flow velocities, and (d) fluid properties, through a comparison of the trapping behavior of H_2 with that of CH_4 and CO_2, on residual trapping by bypassing, which is a key trapping mechanism. Simulation results were supported by a theoretical analysis. The following key conclusions were drawn:

- Residual trapping due to bypassing predominantly occurs at low capillary numbers, emphasizing the role of capillary forces in controlling trapping mechanisms. These results suggest that producing H_2 at higher flow rates will result in less residual trapping, which is in line with experimental findings [65].
- Two types of geometries were studied: rectangular pore doublets and rounded pore doublets. A clear relationship between channel width ratio and trapping percentage was observed, with higher channel width ratios leading to increased trapping. This finding indicates that rocks with a relatively narrow distribution of channel widths are more favorable for UHS, as less H_2 will get trapped due to bypassing. While the use of simplified geometries enabled us to isolate and understand key physical mechanisms, future studies involving more realistic pore structures are needed to confirm and extend these findings.
- The likelihood of trapping is primarily governed by the balance between capillary and viscous forces, making it a useful predictor of the relative extent of trapping in a given system. However, local pore geometry plays a crucial role in determining whether snap-off occurs. Rounded pore geometries reduce trapping, while angular geometries enhance snap-off, leading to increased trapping due to bypassing. Consequently, rocks composed of well-rounded grains are more effective for UHS, whereas angular-grained rocks are less favorable for UHS when considering this trapping mechanism.
- In addition to the capillary number, the mobility ratio plays a key role in predicting residual trapping. H_2 and CH_4 exhibit similar trapping thresholds in terms of capillary number due to their comparable mobility ratios, while CO_2 behaves differently. At similar production rates, H_2 and CH_4 are more prone to trapping by bypassing, whereas CO_2, with its higher viscosity and stronger viscous forces, tends to remain more mobile under the same conditions.

These findings provide valuable insights into the conditions and rock properties that enhance H_2 trapping in subsurface reservoirs, with implications for optimizing underground hydrogen storage strategies.

CRediT authorship contribution statement

Willemijn A. van Rooijen: Writing – original draft, Visualization, Investigation, Formal analysis, Conceptualization. **Pengyu Fu:** Writing – original draft, Software, Methodology, Investigation. **Yuhang Wang:** Writing – review & editing, Supervision, Methodology, Funding acquisition. **Hadi Hajibeygi:** Writing – review & editing, Supervision, Funding acquisition, Conceptualization.

Declaration of competing interest

The authors declare that they have no known competing financial interests or personal relationships that could have appeared to influence the work reported in this paper.

Acknowledgments

Yuhang Wang was supported by the National Natural Science Foundation of China (No. 42307098) and “CUG Scholar” Scientific Research Funds at China University of Geosciences (Wuhan) (Project No. 2022157). Hadi Hajibeygi and Willemijn van Rooijen were sponsored by the Dutch National Science Foundation (NWO) Talent Programme ViDi Project “ADMIRE” (grant number 17509). We thank all ADMIRE members and its user committee for allowing us publish this paper.

Group members of DARSim (Delft Advanced Reservoir Simulation) and ADMIRE (Adaptive Dynamic Multiscale Integrated Reservoir Earth) are acknowledged for fruitful discussions during the development of this work. Additionally, Hadi Hajibeygi and Willemijn van Rooijen acknowledge the Energi Simulation Chair in Subsurface Storage and Multiscale Modeling at TU Delft.

References

[1] IEA. World energy outlook 2025. 2024, URL: www.iea.org/weo. [Accessed 01 February 2025].
[2] United Nations. The Paris agreement. 2015, URL: https://treaties.un.org. [Accessed 01 February 2025].
[3] Dincer I. Renewable energy and sustainable development: a crucial review. Renew Sustain Energy Rev 2000;4(2):157–75. http://dx.doi.org/10.1016/S1364-0321(99)00011-8.
[4] Krevor S, De Coninck H, Gasda SE, Ghaleigh NS, de Gooyert V, Hajibeygi H, Juanes R, Neufeld J, Roberts JJ, Swennenhuis F. Subsurface carbon dioxide and hydrogen storage for a sustainable energy future. Nat Rev Earth Environ 2023;4(2):102–18. http://dx.doi.org/10.1038/s43017-022-00376-8.
[5] Johnston B, Mayo MC, Khare A. Hydrogen: the energy source for the 21st century. Technovation 2005;25:569–85. http://dx.doi.org/10.1016/j.technovation.2003.11.005.
[6] Mahlia T, Saktisahdan T, Jannifar A, Hasan M, Matseelar H. A review of available methods and development on energy storage; technology update. Renew Sustain Energy Rev 2014;33:532–45. http://dx.doi.org/10.1016/j.rser.2014.01.068.
[7] Kovač A, Paranos M, Marciuš D. Hydrogen in energy transition: A review. Int J Hydrog Energy 2021;46:10016–35. http://dx.doi.org/10.1016/j.ijhydene.2020.11.256.
[8] Zhao Q, Wang Y, Chen C. Numerical simulation of the impact of different cushion gases on underground hydrogen storage in aquifers based on an experimentally-benchmarked equation-of-state. Int J Hydrog Energy 2024;50:495–511. http://dx.doi.org/10.1016/j.ijhydene.2023.07.262.
[9] Hashemi L, Blunt MJ, Hajibeygi H. Pore-scale modelling and sensitivity analyses of hydrogen-brine multiphase flow in geological porous media. Sci Rep 2021;11(1):1–13. http://dx.doi.org/10.1038/s41598-021-87490-7.
[10] Andersson J, Grönkvist S. Large-scale storage of hydrogen. Int J Hydrog Energy 2019;44(23):11901–19. http://dx.doi.org/10.1016/j.ijhydene.2019.03.063.
[11] Heinemann N, Alcalde J, Miocic JM, Hangx SJ, Kallmeyer J, Ostertag-Henning C, Hassanpouryouzband A, Thaysen EM, Strobel GJ, Schmidt-Hattenberger C, et al. Enabling large-scale hydrogen storage in porous media–the scientific challenges. Energy Env Sci 2021. http://dx.doi.org/10.1039/D0EE03536J.
[12] Zivar D, Kumar S, Foroozesh J. Underground hydrogen storage: A comprehensive review. Int J Hydrog Energy 2020. http://dx.doi.org/10.1016/j.ijhydene.2020.08.138.
[13] Bo Z, Boon M, Hajibeygi H, Hurter S. Impact of experimentally measured relative permeability hysteresis on reservoir-scale performance of underground hydrogen storage (UHS). Int J Hydrog Energy 2023;48(36):13527–42. http://dx.doi.org/10.1016/j.ijhydene.2022.12.270.
[14] Carden P, Paterson L. Physical, chemical and energy aspects of underground hydrogen storage. Int J Hydrog Energy 1979;4(6):559–69. http://dx.doi.org/10.1016/0360-3199(79)90083-1.
[15] Raza A, Arif M, Glatz G, Mahmoud M, Al Kobaisi M, Alafnan S, Iglauer S. A holistic overview of underground hydrogen storage: Influencing factors, current understanding, and outlook. Fuel 2022;330:125636. http://dx.doi.org/10.1016/j.fuel.2022.125636.
[16] Boon M, Rademaker T, Winardhi CW, Hajibeygi H. Multiscale experimental study of H2/brine multiphase flow in porous rock characterizing relative permeability hysteresis, hydrogen dissolution, and ostwald ripening. Sci Rep 2024;14(1):1–15. http://dx.doi.org/10.1038/s41598-024-81720-4.
[17] Boon M, Hajibeygi H. Experimental characterization of H 2/water multiphase flow in heterogeneous sandstone rock at the core scale relevant for underground hydrogen storage (UHS). Sci Rep 2022;12(1):14604. http://dx.doi.org/10.1038/s41598-022-18759-8.
[18] Al-Yaseri A, Yekeen N, Al-Mukainah H, Sarmadivaleh M, Lebedev M. Snap-off effects and high hydrogen residual trapping: Implications for underground hydrogen storage in sandstone aquifer. Energy Fuels 2024. http://dx.doi.org/10.1021/acs.energyfuels.3c04261.
[19] Higgs S, Da Wang Y, Sun C, Ennis-King J, Jackson SJ, Armstrong RT, Mostaghimi P. Comparative analysis of hydrogen, methane and nitrogen relative permeability: Implications for underground hydrogen storage. J Energy Storage 2023;73:108827. http://dx.doi.org/10.1016/j.est.2023.108827.
[20] Al-Yaseri A, Esteban L, Giwelli A, Sarout J, Lebedev M, Sarmadivaleh M. Initial and residual trapping of hydrogen and nitrogen in fontainebleau sandstone using nuclear magnetic resonance core flooding. Int J Hydrog Energy 2022;47(53):22482–94. http://dx.doi.org/10.1016/j.ijhydene.2022.05.059.
[21] Lysyy M, Liu N, Solstad CM, Fernø MA, Ersland G. Microfluidic hydrogen storage capacity and residual trapping during cyclic injections: Implications for underground storage. Int J Hydrog Energy 2023;48(80):31294–304. http://dx.doi.org/10.1016/j.ijhydene.2023.04.253.
[22] Jha NK, Al-Yaseri A, Ghasemi M, Al-Bayati D, Lebedev M, Sarmadivaleh M. Pore scale investigation of hydrogen injection in sandstone via X-ray microtomography. Int J Hydrog Energy 2021;46(70):34822–9. http://dx.doi.org/10.1016/j.ijhydene.2021.08.042.
[23] Jangda Z, Menke H, Busch A, Geiger S, Bultreys T, Lewis H, Singh K. Pore-scale visualization of hydrogen storage in a sandstone at subsurface pressure and temperature conditions: Trapping, dissolution and wettability. J Colloid Interface Sci 2023;629:316–25. http://dx.doi.org/10.1016/j.jcis.2022.09.082.
[24] Krevor S, Blunt MJ, Benson SM, Pentland CH, Reynolds C, Al-Menhali A, Niu B. Capillary trapping for geologic carbon dioxide storage–From pore scale physics to field scale implications. Int J Greenh Gas Control 2015;40:221–37. http://dx.doi.org/10.1016/j.ijggc.2015.04.006.
[25] Yu S, Hu M, Steefel CI, Battiato I. Unraveling residual trapping for geologic hydrogen storage and production using pore-scale modeling. Adv Water Resour 2024;104659. http://dx.doi.org/10.1016/j.advwatres.2024.104659.
[26] Chatzis I, Morrow NR, Lim HT. Magnitude and detailed structure of residual oil saturation. Soc Pet Eng J 1983;23(02):311–26. http://dx.doi.org/10.2118/10681-PA.
[27] Ni H, Boon M, Garing C, Benson SM. Predicting CO_2 residual trapping ability based on experimental petrophysical properties for different sandstone types. Int J Greenh Gas Control 2019;86:158–76. http://dx.doi.org/10.1016/j.ijggc.2019.04.024.
[28] Rose W, Witherspoon PA. Studies of waterflood performance II. Trapping oil in a pore doublet. 1956, Circ No. 224.
[29] Rose W, Cleary J. Further indications of pore doublet theory. Prod Mon 1958;22(3):20–5.
[30] Moore T, Slobod R. Displacement of oil by water-effect of wettability, rate, and viscosity on recovery. In: SPE annual technical conference and exhibition. SPE; 1955, p. SPE–502. http://dx.doi.org/10.2118/502-G.
[31] Dullien FA. Porous media: fluid transport and pore structure. Academic Press; 2012.
[32] Chatzis I, Dullien F. Dynamic immiscible displacement mechanisms in pore doublets: theory versus experiment. J Colloid Interface Sci 1983;91(1):199–222. http://dx.doi.org/10.1016/0021-9797(83)90326-0.
[33] van Rooijen WA, Hashemi L, Boon M, Farajzadeh R, Hajibeygi H. Microfluidics-based analysis of dynamic contact angles relevant for underground hydrogen storage. Adv Water Resour 2022;164:104221. http://dx.doi.org/10.1016/j.advwatres.2022.104221.
[34] Shan F, Chai Z, Shi B, Zhao M. Optimal displacement of immiscible two-phase fluids in a pore doublet. Phys Fluids 2023;35(5). http://dx.doi.org/10.1063/5.0149182.
[35] Gu Q, Liu H, Wu L. Preferential imbibition in a dual-permeability pore network. J Fluid Mech 2021;915:A138. http://dx.doi.org/10.1017/jfm.2021.174.
[36] Chatzis I, Kuntamukkula M, Morrow N. Effect of capillary number on the microstructure of residual oil in strongly water-wet sandstones. SPE Reserv Eng 1988;3(03):902–12. http://dx.doi.org/10.2118/13213-PA.
[37] Stegemeier GL. Relationship of trapped oil saturation to petrophysical properties of porous media. In: SPE improved oil recovery conference. SPE; 1974, p. SPE–4754. http://dx.doi.org/10.2118/4754-MS.
[38] Herring AL, Gilby F, Li Z, McClure J, Turner M, Veldkamp J, Beeching L, Sheppard A. Observations of nonwetting phase snap-off during drainage. Adv Water Resour 2018;121:32–43. http://dx.doi.org/10.1016/j.advwatres.2018.07.016.
[39] Pentland CH, El-Maghraby R, Georgiadis A, Iglauer S, Blunt MJ. Immiscible displacements and capillary trapping in CO_2 storage. Energy Procedia 2011;4:4969–76. http://dx.doi.org/10.1016/j.egypro.2011.02.467.
[40] Shi J-Q, Xue Z, Durucan S. Supercritical CO_2 core flooding and imbibition in Berea sandstone—CT imaging and numerical simulation. Energy Procedia 2011;4:5001–8. http://dx.doi.org/10.1016/j.egypro.2011.02.471.
[41] Mehmani A, Kelly S, Torres-Verdín C, Balhoff M. Capillary trapping following imbibition in porous media: Microfluidic quantification of the impact of pore-scale surface roughness. Water Resour Res 2019;55(11):9905–25. http://dx.doi.org/10.1029/2019WR025170.
[42] Buchgraber M, Kovscek AR, Castanier LM. A study of microscale gas trapping using etched silicon micromodels. Transp Porous Media 2012;95:647–68. http://dx.doi.org/10.1007/s11242-012-0067-0.
[43] Yekta AE, Manceau J-C, Gaboreau S, Pichavant M, Audigane P. Determination of hydrogen–water relative permeability and capillary pressure in sandstone: application to underground hydrogen injection in sedimentary formations. Transp Porous Media 2018;122(2):333–56. http://dx.doi.org/10.1007/s11242-018-1004-7.
[44] Berg S, Rücker M, Ott H, Georgiadis A, Van der Linde H, Enzmann F, Kersten M, Armstrong RT, De With S, Becker J, et al. Connected pathway relative permeability from pore-scale imaging of imbibition. Adv Water Resour 2016;90:24–35. http://dx.doi.org/10.1016/j.advwatres.2016.01.010.

[45] Blunt MJ. Multiphase flow in permeable media: A pore-scale perspective. Cambridge University Press; 2017.
[46] Zheng J, Lei W, Ju Y, Wang M. Investigation of spontaneous imbibition behavior in a 3D pore space under reservoir condition by lattice Boltzmann method. J Geophys Res: Solid Earth 2021;126(6). http://dx.doi.org/10.1029/2021JB021987, e2021JB021987.
[47] Joekar-Niasar V, Doster F, Armstrong R, Wildenschild D, Celia MA. Trapping and hysteresis in two-phase flow in porous media: A pore-network study. Water Resour Res 2013;49(7):4244–56. http://dx.doi.org/10.1002/wrcr.20313.
[48] Alizadeh M, Fatemi M. Pore-doublet computational fluid dynamic simulation of the effects of dynamic contact angle and interfacial tension alterations on the displacement mechanisms of oil by low salinity water. Int J Multiph Flow 2021;143:103771. http://dx.doi.org/10.1016/j.ijmultiphaseflow.2021.103771.
[49] Raeini AQ, Bijeljic B, Blunt MJ. Numerical modelling of sub-pore scale events in two-phase flow through porous media. Transp Porous Media 2014;101:191–213. http://dx.doi.org/10.1007/s11242-013-0239-6.
[50] Nabizadeh A, Adibifard M, Hassanzadeh H, Fahimpour J, Moraveji MK. Computational fluid dynamics to analyze the effects of initial wetting film and triple contact line on the efficiency of immiscible two-phase flow in a pore doublet model. J Mol Liq 2019;273:248–58. http://dx.doi.org/10.1016/j.molliq.2018.10.029.
[51] Mehmani Y, Anderson T, Wang Y, Aryana SA, Battiato I, Tchelepi HA, Kovscek AR. Striving to translate shale physics across ten orders of magnitude: What have we learned? Earth-Sci Rev 2021;223:103848.
[52] Wang J, Yang Y, Cai S, Yao J, Xie Q. Pore-scale modelling on hydrogen transport in porous media: Implications for hydrogen storage in saline aquifers. Int J Hydrog Energy 2023;48(37):13922–33. http://dx.doi.org/10.1016/j.ijhydene.2022.11.299.
[53] Chen S, Doolen GD. Lattice Boltzmann method for fluid flows. Annu Rev Fluid Mech 1998;30(1):329–64. http://dx.doi.org/10.1146/annurev.fluid.30.1.329.
[54] Sussman M, Smereka P, Osher S. A level set approach for computing solutions to incompressible two-phase flow. J Comput Phys 1994;114(1):146–59. http://dx.doi.org/10.1006/jcph.1994.1155.
[55] Youngs DL. Time-dependent multi-material flow with large fluid distortion. Numer Methods Fluid Dyn 1982.
[56] Tavares M, Josserand C, Limare A, Lopez-Herrera JM, Popinet S. A coupled VOF/embedded boundary method to model two-phase flows on arbitrary solid surfaces. Comput Fluids 2024;106317. http://dx.doi.org/10.1016/j.compfluid.2024.106317.
[57] Chen L, Kang Q, Mu Y, He Y-L, Tao W-Q. A critical review of the pseudopotential multiphase lattice Boltzmann model: Methods and applications. Int J Heat Mass Transfer 2014;76:210–36. http://dx.doi.org/10.1016/j.ijheatmasstransfer.2014.04.032.
[58] Ramstad T, Idowu N, Nardi C, Øren P-E. Relative permeability calculations from two-phase flow simulations directly on digital images of porous rocks. Transp Porous Media 2012;94(2):487–504. http://dx.doi.org/10.1007/s11242-011-9877-8.
[59] Huang H, Li Z, Liu S, Lu X-y. Shan-and-Chen-type multiphase lattice Boltzmann study of viscous coupling effects for two-phase flow in porous media. Internat J Numer Methods Fluids 2009;61(3):341–54. http://dx.doi.org/10.1002/fld.1972.
[60] Wang Y, Aryana SA. Pore-scale simulation of gas flow in microscopic permeable media with complex geometries. J Nat Gas Sci Eng 2020;81:103441. http://dx.doi.org/10.1016/j.jngse.2020.103441.
[61] Wang Y, Chakrapani TH, Wen Z, Hajibeygi H. Pore-scale simulation of H_2-brine system relevant for underground hydrogen storage: A lattice Boltzmann investigation. Adv Water Resour 2024;104756. http://dx.doi.org/10.1016/j.advwatres.2024.104756.
[62] Song H, Zhou Y, Xie Z, Lao J, Yue M. A pore-scale simulation of the effect of heterogeneity on underground hydrogen storage. Water 2024;16(22):3264. http://dx.doi.org/10.3390/w16223264.
[63] Lysyy M, Ersland G, Fernø M. Pore-scale dynamics for underground porous media hydrogen storage. Adv Water Resour 2022;163:104167. http://dx.doi.org/10.1016/j.advwatres.2022.104167.
[64] Zhao Q, Wang H, Chen C. Underground hydrogen storage: a recovery prediction using pore network modeling and machine learning. Fuel 2024;357:130051. http://dx.doi.org/10.1016/j.fuel.2023.130051.
[65] Thaysen EM, Butler IB, Hassanpouryouzband A, Freitas D, Alvarez-Borges F, Krevor S, Heinemann N, Atwood R, Edlmann K. Pore-scale imaging of hydrogen displacement and trapping in porous media. Int J Hydrog Energy 2023;48(8):3091–106. http://dx.doi.org/10.1016/j.ijhydene.2022.10.153.
[66] Bagheri M, Mahani H, Ayatollahi S, Zivar D. Direct pore-scale simulation of the effect of capillary number and gas compressibility on cyclic underground hydrogen storage & production in heterogeneous aquifers. Adv Water Resour 2023;181:104547. http://dx.doi.org/10.1016/j.advwatres.2023.104547.
[67] Liu H, Valocchi AJ, Werth C, Kang Q, Oostrom M. Pore-scale simulation of liquid CO_2 displacement of water using a two-phase lattice Boltzmann model. Adv Water Resour 2014;73:144–58. http://dx.doi.org/10.1016/j.advwatres.2014.07.010.
[68] Xu Z, Liu H, Valocchi AJ. Lattice Boltzmann simulation of immiscible two-phase flow with capillary valve effect in porous media. Water Resour Res 2017;53(5):3770–90. http://dx.doi.org/10.1002/2017WR020373.
[69] Gunstensen AK, Rothman DH, Zaleski S, Zanetti G. Lattice Boltzmann model of immiscible fluids. Phys Rev A 1991;43(8):4320. http://dx.doi.org/10.1103/PhysRevA.43.4320.
[70] d'Humières D. Generalized lattice-Boltzmann equations. In: Shizgal BD, Weaver DP, editors. In: Rarefied gas dynamics: theory and simulations, vol. 159, Washington, DC: AIAA; 1992, p. 450–8. http://dx.doi.org/10.2514/5.9781600866319.0450.0458.
[71] Lallemand P, Luo L-S. Theory of the lattice Boltzmann method: Dispersion, dissipation, isotropy, Galilean invariance, and stability. Phys Rev E 2000;61:6546–62. http://dx.doi.org/10.1103/PhysRevE.61.6546.
[72] Chai Z, Shi B. Multiple-relaxation-time lattice Boltzmann method for the Navier-Stokes and nonlinear convection-diffusion equations: Modeling, analysis, and elements. Phys Rev E 2020;102(2):023306. http://dx.doi.org/10.1103/PhysRevE.102.023306.
[73] d'Humières D, Ginzburg I, Krafczyk M, Lallemand P, Luo L. Multiple-relaxation-time lattice Boltzmann models in three dimensions. Philos Trans R Soc A 2002;360(1792):437–51. http://dx.doi.org/10.1098/rsta.2001.0955.
[74] Yu Z, Fan L-S. Multirelaxation-time interaction-potential-based lattice Boltzmann model for two-phase flow. Phys Rev E 2010;82:046708. http://dx.doi.org/10.1103/PhysRevE.82.046708.
[75] Guo Z, Zheng C, Shi B. Discrete lattice effects on the forcing term in the lattice Boltzmann method. Phys Rev E 2002;65:046308. http://dx.doi.org/10.1103/PhysRevE.65.046308.
[76] Brackbill JU, Kothe DB, Zemach C. A continuum method for modeling surface tension. J Comput Phys 1992;100(2):335–54. http://dx.doi.org/10.1016/0021-9991(92)90240-Y.
[77] Lishchuk SV, Care CM, Halliday I. Lattice Boltzmann algorithm for surface tension with greatly reduced microcurrents. Phys Rev E 2003;67:036701. http://dx.doi.org/10.1103/PhysRevE.67.036701.
[78] Latva-Kokko M, Rothman DH. Diffusion properties of gradient-based lattice Boltzmann models of immiscible fluids. Phys Rev E 2005;71:056702. http://dx.doi.org/10.1103/PhysRevE.71.056702.
[79] Iglauer S. Optimum geological storage depths for structural H_2 geo-storage. J Pet Sci Eng 2022;212:109498. http://dx.doi.org/10.1016/j.petrol.2021.109498.
[80] Hashemi L, Glerum W, Farajzadeh R, Hajibeygi H. Contact angle measurement for hydrogen/brine/sandstone system using captive-bubble method relevant for underground hydrogen storage. Adv Water Resour 2021;154:103964. http://dx.doi.org/10.1016/j.advwatres.2021.103964.
[81] Hashemi L, Boon M, Glerum W, Farajzadeh R, Hajibeygi H. A comparative study for H_2–CH_4 mixture wettability in sandstone porous rocks relevant to underground hydrogen storage. Adv Water Resour 2022;163:104165. http://dx.doi.org/10.1016/j.advwatres.2022.104165.
[82] Haeri F, Tapriyal D, Sanguinito S, Shi F, Fuchs SJ, Dalton LE, Baltrus J, Howard B, Crandall D, Matranga C, et al. CO_2-brine contact angle measurements on navajo, nugget, bentheimer, bandera brown, berea, and mt. simon sandstones. Energy Fuels 2020;34(5):6085–100. http://dx.doi.org/10.1021/acs.energyfuels.0c00436.
[83] Zhao Q, Guo R, Jha NK, Sarmadivaleh M, Lebedev M, Al-Yaseri A, McClure J, Chen C. Using X-ray computed tomography and pore-scale numerical modeling to study the role of heterogeneous rock surface wettability on hydrogen-brine two-phase flow in underground hydrogen storage. Fuel 2024;366:131414. http://dx.doi.org/10.1016/j.fuel.2024.131414.
[84] Zhao J, Qin F, Fischer R, Kang Q, Derome D, Carmeliet J. Spontaneous imbibition in a square tube with corner films: Theoretical model and numerical simulation. Water Resour Res 2021;57(2). http://dx.doi.org/10.1029/2020WR029190, e2020WR029190.
[85] Lemmon EW, Huber ML, McLinden MO. NIST reference fluid thermodynamic and transport properties–REFPROP. NIST Stand Ref Database 2002;23(2002):v7.
[86] Laliberté M, Cooper WE. Model for calculating the density of aqueous electrolyte solutinos. J Chem Eng Data 2004;49:1141–51. http://dx.doi.org/10.1021/je0498659.
[87] Laliberté M. Model for calculating the viscosity of aqueous solutions. J Chem Eng Data 2007;52:321–35. http://dx.doi.org/10.1021/JE0604075.
[88] Van Rooijen WA, Habibi P, Xu K, Dey P, Vlugt TJH, Hajibeygi H, Moultos OA. Interfacial tensions, solubilities, and transport properties of the H_2/H_2O/NaCl system: A molecular simulation study. J Chem Eng Data 2023. http://dx.doi.org/10.1021/acs.jced.2c00707.
[89] Mirchi V, Dejam M, Alvarado V. Interfacial tension and contact angle measurements for hydrogen-methane mixtures/brine/oil-wet rocks at reservoir conditions. Int J Hydrog Energy 2022;47(82):34963–75. http://dx.doi.org/10.1016/j.ijhydene.2022.08.056.
[90] Niu Q, Dong Z, Lv Q, Zhang F, Shen H, Yang Z, Lin M, Zhang J, Xiao K. Role of interfacial and bulk properties of long-chain viscoelastic surfactant in stabilization mechanism of CO_2 foam for CCUS. J CO2 Util 2022;66:102297. http://dx.doi.org/10.1016/j.jcou.2022.102297.
[91] Wang Z. Immiscible fluid displacement: From pore doublets to porous media. Capillarity 2025;15(1):1–3. http://dx.doi.org/10.46690/capi.2025.04.01.
[92] Zou Q, He X. On pressure and velocity boundary conditions for the lattice Boltzmann BGK model. Phys Fluids 1997;9(6):1591–8. http://dx.doi.org/10.1063/1.869307.

[93] Zong Y, Li M, Wang K. Outflow boundary condition of multiphase microfluidic flow based on phase ratio equation in lattice Boltzmann method. Phys Fluids 2021;33(7):073304. http://dx.doi.org/10.1063/5.0058045.
[94] Ladd A. Numerical simulations of particulate suspensions via a discretized Boltzmann equation. Part 1. Theoretical foundation. J Fluid Mech 1994;271:285–309. http://dx.doi.org/10.1017/S0022112094001771.
[95] Ladd A. Numerical simulations of particulate suspensions via a discretized Boltzmann equation. Part 2. Numerical results. J Fluid Mech 1994;271:311–39. http://dx.doi.org/10.1017/S0022112094001783.
[96] Gomez Mendez I, El-Sayed WM, Menefee AH, Karpyn ZT. Insights into underground hydrogen storage challenges: A review on hydrodynamic and biogeochemical experiments in porous media. Energy Fuels 2024;38(21):20015–32. http://dx.doi.org/10.1021/acs.energyfuels.4c03142.
[97] Moore T, Slobod R. The effect of viscosity and capillarity on the displacement of oil by water. Prod Mon 1956;20(10):20–30. http://dx.doi.org/10.2118/502-G.
[98] Morrow NR, Chatzis I, Taber J. Entrapment and mobilization of residual oil in bead packs. SPE Res Eng 1988;3(03):927–34. http://dx.doi.org/10.2118/14423-PA.
[99] Suekane T, Zhou N, Hosokawa T, Matsumoto T. Direct observation of trapped gas bubbles by capillarity in sandy porous media. Transp Porous Media 2010;82:111–22. http://dx.doi.org/10.1007/s11242-009-9439-5.
[100] Herring AL, Harper EJ, Andersson L, Sheppard A, Bay BK, Wildenschild D. Effect of fluid topology on residual nonwetting phase trapping: Implications for geologic CO_2 sequestration. Adv Water Resour 2013;62:47–58. http://dx.doi.org/10.1016/j.advwatres.2013.09.015.
[101] Hughes RG, Blunt MJ. Pore scale modeling of rate effects in imbibition. Transp Porous Media 2000;40:295–322. http://dx.doi.org/10.1023/A:1006629019153.
[102] Hassanpouryouzband A, Wilkinson M, Haszeldine RS. Hydrogen energy futures – foraging or farming? Chem Soc Rev 2024;53:2258–63. http://dx.doi.org/10.1039/D3CS00723E.
[103] Hassanpouryouzband A, Jahanbani Veshareh M, Wilkinson M, Nick HM, Ngwenya BT, Haszeldine RS. In situ hydrogen generation from underground fossil hydrocarbons. Joule 2025. http://dx.doi.org/10.1016/j.joule.2024.101809.